J. Nanoanalysis., 7(4): -17, Autumn 2020

RESEARCH ARTICLE

High efficient solar light photocatalytic degradation of malachite green by solid state synthesized $Bi_2Sn_2O_7$ and $Bi_2M_xSn_2O_7$ (M = Y^{3+}, Eu^{3+}, Gd^{3+} and Yb^{3+}) nanomaterials

Ladan Roohandeh[1], Alireza Hakimyfard[1,], Mohammad Samimifar[2]*

[1]Department of Physics, Faculty of Science, Jundi-Shapur University of Technology, Dezful, Iran

[2]Department of Chemistry, Faculty of Science, Jundi-Shapur University of Technology, Dezful, Iran

ARTICLE INFO

Article History:
Received 2020-02-22
Accepted 2020-04-04
Published 2020-10-01

Keywords:
photodegradation, Solid state, Rietveld, Kinetic, pyrochlore.

ABSTRACT

Nanostructured $Bi_2Sn_2O_7$ and $Bi_2M_xSn_2O_7$ (M = Y^{3+}, Eu^{3+}, Gd^{3+} and Yb^{3+}) nanomaterials were synthesized by conventional one-step solid state crystal growth reactions among Bi(NO3)3, SnCl2 and M2O3 raw materials at 800̊ C for 10 and 15 h. The doped nanomaterials were synthesized to study the capacity of the crystal system to locate each of the dopant ions into the crystal system cavities. The synthesized nanomaterials were characterized by powder X-ray diffraction (PXRD) technique. Rietveld analysis showed that the obtained materials were crystallized well in orthorhombic crystal structure with the space group Aba2. The PXRD data revealed that dopant ion type had a considerable influence on the crystal phase purity of the obtained targets. The morphologies of the synthesized materials were studied by field emission scanning electron microscopy (FESEM) technique. Ultraviolet-visible spectra analysis showed that the synthesized nanomaterials had strong light absorption in the ultraviolet light region. Photocatalytic performance of the synthesized nanomaterials was investigated for the degradation of pollutant Malachite Green under solar light condition. The optimum conditions were modeled and obtained by design expert software for Bi2Sn2O7 that was synthesized at 800̊ C for 10 h which were 0.06 mL H_2O_2, 12 mg catalyst and 40 min for the removal of 50 mL of 40 ppm MG solution. The degradation yield in these conditions was 100 %. The photocatalytic degradation fitted to the Langmuir–Hinshelwood kinetic model. As a result of the model, the kinetic of degradation followed a pseudo-zero-order kinetic model.

How to cite this article
*Roohandeh L., Hakimyfard A.R., Samimifar M. High efficient solar light photocatalytic degradation of malachite green by solid state synthesized $Bi_2Sn_2O_7$ and $Bi_2M_xSn_2O_7$ (M = Y^{3+}, Eu^{3+}, Gd^{3+} and Yb^{3+}) nanomaterials. J. Nanoanalysis., 2020; 7(4): -17. DOI: 10.22034/jna.***.*

INTRODUCTION

Mixed metal oxides with general formula $A_2B_2O_7$ (A is a medium-large cation and B is an octahedrally coordinated, high charge cation) have been widely studied for their potential applications [1-3]. The Pyrochlore-type $Bi_2Sn_2O_7$ was first reported by Roth [4]. The pyrochlore structure is formed when the ionic radius ratio of the two cations (A/B) lies between 1.46 and 1.78. In the case of $Bi_2Sn_2O_7$, the radius ratio is 1.70 [5]. So, $Bi_2Sn_2O_7$ belongs to the pyrochlore family of general formula $A_2B_2O_7$ [6]. $Bi_2Sn_2O_7$ shows certain photocatalytic ability in the visible light range. The direct optical band gap value of $Bi_2Sn_2O_7$ is 2.3–2.8 eV [7,8]. $Bi_2Sn_2O_7$ is a desirable ternary oxide showing utility in a wide array of organic transformations and acts as a selective CO-sensing device [9,10]. So, $Bi_2Sn_2O_7$ has found applications in gas-sensing devices as a selective sensor for carbon monoxide in the presence of other gases [11,12]. $Bi_2Sn_2O_7$ is not only a key component of multiphasic catalyst for isobutene-to-methacrolein conversion [13], but it has also been utilized as a catalyst in several reactions such as oxidative dehydrodimerization of propylene [14], oxidative dehydroaromatization of isobutene [15], and oxidative coupling of methane [16,17]. Besides, bismuth-containing oxides are

---

* Corresponding Author Email: *ahakimyfard@jsu.ac.ir*

of considerable importance as heterogeneous catalysts for a variety of processes and also are used as electrode materials in the reduction of oxygen [18]. The photocatalytic property of the pyrochlore compound is enhanced with doping with rare earth ions that can reduce the recombination rate of electron-hole pairs and enhance the interfacial charge transfer efficiency [19]. Previous experimental investigations have confirmed that $Bi_2Sn_2O_7$ has three polymorphs. At room temperature, $Bi_2Sn_2O_7$ adopts a monoclinic structure and is designated as α phase. At intermediate temperature higher than 90 ◦C, orthorhombic phase (β phase) is found. At temperature above 680 ◦C, $Bi_2Sn_2O_7$ is the ideal pyrochlore structure with cubic symmetry and designated as the γ phase [20]. β-$Bi_2Sn_2O_7$ has orthorhombic crystal structure with space group Aba2 and unit cell parameters a = 7.571833(8), b = 21.41262(2), and c = 15.132459(14) Å. α-$Bi_2Sn_2O_7$ has monoclinic crystal structure with space group Cc and unit cell parameters a = 13.15493(6), b = 7.54118(4), and c = 15.07672(7) Å and β = 125.0120(3)° [21]. The other crystal system reported in the literature is the cubic crystal system with the space group Fd-3m and the lattice parameter a = b = c = 10.7 Å [22]. In $Bi_2Sn_2O_7$ crystal phases, α-$Bi_2Sn_2O_7$ is mentioned as a catalyst in several partial oxidation reactions such as dehydrodimerization or aromatic dehydroaromatization of propene, selective oxidation of propene into acrolein, oxidative dehydrogenation of 1-butene into butadiene and oxidative coupling of methane [23]. However, β-phase has a band gap energy of 2.3 eV, which is lower than that of the α-phase (2.85 eV). But the α phase is considered as a catalyst because it has a high quantum efficiency thus offering low-speed recombination of photo generated electron–hole pairs [24]. So, until now, there is no reported published work considers β-$Bi_2Sn_2O_7$ as a photocatalyst. Several methods have been reported for the synthesis of $Bi_2Sn_2O_7$ materials such as hydrothermal [4,25,4,7,17, 26, 27-30], thermal decomposition of complex [10], chemical co-precipitation [8], solving metal oxides in organic solvent and heating at 800 ℃ for 24 h [23], organic solution and heating at 800 ℃ for 20 h [27], solid state at 1000 ℃ for 4 days [18], solid state at 1000 ℃ for 16 h [21], solid state using Bi_2O_3, SnO_2 at 800 – 900 ℃ for 8 h and then 1050 ℃ for 2 h. A cubic crystal system was obtained by this method [22], solid state using Bi_2O_3, SnO_2 mixed in a liquid medium and calcined at 800 ℃ for 8 h and then at 900℃ for 8 h in silica crucible under air atmosphere. The obtained $Bi_2Sn_2O_7$ had cubic crystal phase [31]; solid state gas phase using Sn and Bi powders raw materials at 700 – 900 ℃. In this case, a tetragonal crystal system was obtained [32]; solid-state using Bi_2O_3 and SnO_2 at 1100 ℃. In the process, a cubic crystal system was achieved [33]; solid state at 800 ℃ for 24 h and then 48 h reaction using SnO_2 and Bi_2O_3; a cubic crystal phase was obtained [34]; Solid state by heating SnO_2 and Bi_2O_3 mixtures for 24 h at 900 to 1000°C in gold lined Al_2O_3 crucible. Cubic and tetragonal crystal systems were obtained [35]; solid state using Bi_2O_3 and SnO_2 at 750 ℃ for 12-24 h. Monoclinic and cubic phase distributions at different temperatures were achieved [36]; solid state using Bi_2O_3 and SnO_2 at 750 – 950 ℃ for 8 to 24 h. A mixture of cubic and orthorhombic crystal system was obtained [37]; solid state using Bi_2O_3 and SnO_2 at 1100 ℃ and a tetragonal crystal system was obtained [38], etc.

A photocatalytic application for removing MG from aqueous waste water is also reported in the present work. MG is a triarylamine dye and used in pigment industry. MG is used in leather, paper, silk, cotton, and jute dyeing processes. It is also used as an antifungal and anti-protozoan agent in fisheries and aquaculture industry [39,40]. It is a non-biodegradable dye pollutant and is a highly controversial compound. Furthermore, MG and its metabolites are known to cause mutagenic, carcinogenic, and teratogenic effects to live organisms [41]. It should not be used for beverages, food, medicines. Its inhalation may irritate the respiratory tract, and in large quantities causes tissue damage and inflammation of kidneys [42,43]. Recently, several metal oxides and sulfides have been used for the degradation of MG under different conditions summarized in ref. [44,45].

The present work reports a conventional one-step solid state method for the synthesis of β-$Bi_2Sn_2O_7$ and $Bi_2M_xSn_2O_7$ (M = Y^{3+}, Eu^{3+}, Gd^{3+} and Yb^{3+}) nanomaterials using $Bi(NO_3)_3$, $SnCl_2$, Y_2O_3, Eu_2O_3, Gd_2O_3 and Yb_2O_3 raw materials at 800 ℃ for 10 and 15 h. Rietveld analysis data are used to calculate the variation of the crystallographic parameters of the obtained materials when the reaction time and the dopant ion are changed. Besides, the band gap energies of the as-prepared pure and doped nanomaterials are initially estimated from ultraviolet-visible spectra. FESEM images are also used to study the morphology changes of the obtained targets when the reaction time and the dopant type are changed. Besides, the photocatalytic application of the synthesized $Bi_2Sn_2O_7$ nanomaterial is also investigated for the degradation of MG under solar light conditions. The experimental design method is used to optimize the factors affecting the degradation process. The parameters are the amount of the nanocatalyst, H_2O_2 and the reaction time. The data show that the synthesized $Bi_2Sn_2O_7$ nanocatalyst has very good efficiency at aqueous solution under the optimized conditions.

EXPERIMENTAL

General remarks

All chemicals were of analytical grade, obtained from commercial sources, and used without further purification. Phase identifications were performed on a powder X-ray diffractometer D5000 (Siemens AG, Munich, Germany) using CuKa radiation. The Rietveld analysis was performed by FullProf software. The morphology of the obtained materials was examined with a Philips XL30 scanning electron microscope (Philips, Amsterdam, Netherlands) equipped with an energy-dispersive X-ray (EDX) spectrometer. FTIR spectra were recorded on a Tensor 27 (Bruker Corporation, Germany). Absorption spectra were recorded on an Analytik Jena Specord 40 (Analytik Jena AG Analytical Instrumentation, Jena, Germany). For the photocatalytic degradation, the test solutions were prepared daily by solving certain amount of the solid MG dye in the deionized distilled water. The MG concentration of MG was determined at 606 nm using a Shimadzu UV-visible1650 PC spectrophotometer. A BEL PHS-3BW pH-meter with a combined glass-Ag/AgCl electrode was used for adjustment of the solution pH.

Synthesis of $Bi_2Sn_2O_7$ nano-photocatalyst

In a typical synthetic experiment, 0.243 g (0.5 mmol) of $Bi(NO_3)_3$ (Mw = 485.08 g mol^{-1}) and 0.113 g (0.5 mmol) of $SnCl_2$ (Mw = 225.5 g mol^{-1}) were mixed in a mortar and ground until a nearly homogeneous powder was obtained. The obtained powder was added into a 25 mL crucible and treated thermally in one step in a pre-heated electrical oven at 800 ℃ for 10 (S_1) or 15 h (S_2). The crucible was then cooled normally in oven to the room temperature. The obtained powder was collected for further analyses. The synthesis yield for $Bi_2Sn_2O_7$ (Mw = 767.4 g mol^{-1}) was 0.34 g (89 %) and 0.35 g (91 %) for S_1 and S_2, respectively.

Synthesis of $Bi_2M_xSn_2O_7$ (M= Y^{3+}, Eu^{3+}, Gd^{3+} and Yb^{3+}) (x=mmol of dopant ion) nanomaterials

For the synthesis of the doped materials, 0.5 mmol of $Bi(NO_3)_3$, 0.5 mmol of $SnCl_2$ and 0.01 g of Y_2O_3 (S_3), or Eu_2O_3 (S_4), or Gd_2O_3 (S_5) and/or Yb_2O_3 (S_6) were mixed in a mortar and ground until a nearly homogeneous powder was obtained. The obtained powder was added into a 25 mL crucible and treated thermally in one step at 800 ℃ for 15. The crucible was then cooled normally in oven to the room temperature. The obtained powder was collected for further analyses. The powder weight amount for the doped $Bi_2Sn_2O_7$ was 0.21 g, 0.31 g, 0.26 g and 0.29 g for S_3, S_4, S_5 and S_6, respectively.

RESULT AND DISCUSSION

Characterization

The phase composition of the as-prepared $Bi_2Sn_2O_7$ and $Bi_2M_xSn_2O_7$ (M= Y^{3+}, Eu^{3+}, Gd^{3+} and Yb^{3+}) nanomaterials was examined by powder X-ray diffraction technique. Figs. 1 and 2 show the PXRD patterns of the obtained materials in the 2θ range 10–80°. The results of the structural analysis performed by the *FullProf* program employing profile matching with constant scale factors are also included in the Figs. Red lines are the observed intensities while the black ones are the calculated data. The blue line is the difference: Y_{obs} - Y_{calc}. The Bragg reflection positions are indicated by blue bars for the main crystal phase ($Bi_2Sn_2O_7$) and red bars for the impurity crystal phase. Fig. 1 a-c shows a comparison study of the crystal system type of the obtained target. It was found that when the crystallographic parameters of cubic crystal system including Fd-3m space group with a=b=c= 10.7 Å [22] is used in the rietveld analysis, some impurity peaks marked with *have appeared. Besides, the impurity peaks are still present when the crystallographic parameters of the monoclinic crystal system is included in the rietveld analysis (Space group = Cc, a=13.08907 Å, b = 7.53348 Å and c = 15.02513 Å and β = 125°) [21]. However, when orthorhombic crystallographic parameters are included in the rietveld analysis (space group = Aba2, a = 7.54632 Å, b = 21.51632 Å and c = 15.08011 Å) [21], no impurity peak was observed. Table 1 shows the rietveld analyses data of S_2. The table shows that the refinement of S_2 is good when the crystallographic data of orthorhombic crystal system is used in the rietveld analysis. So

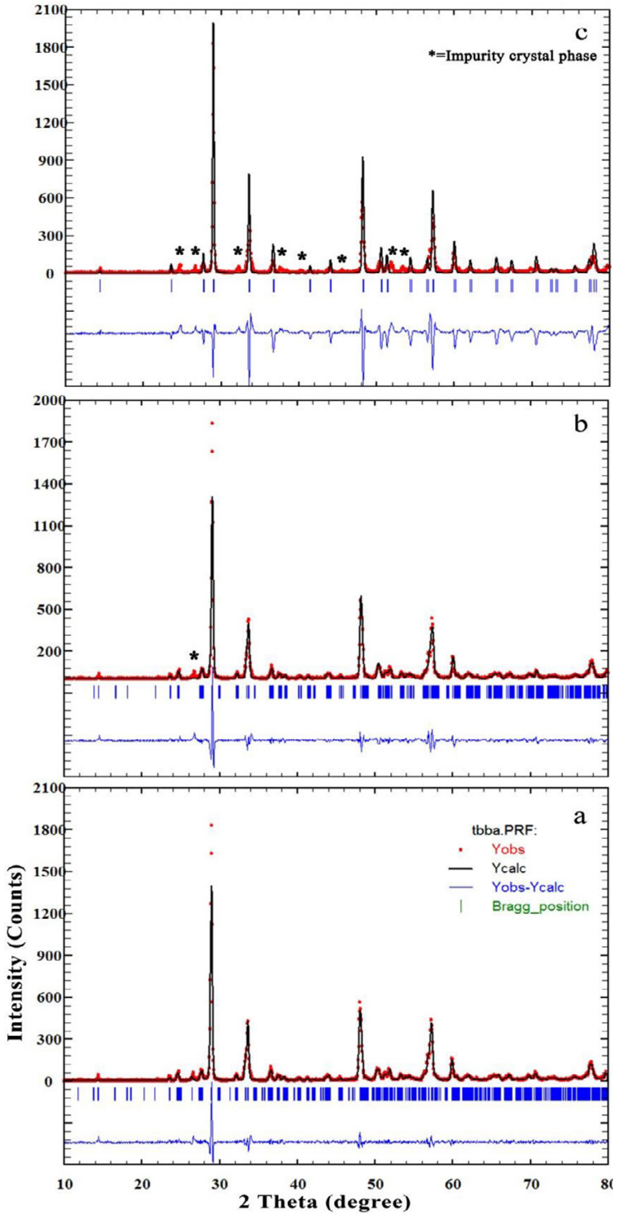

Fig. 1. A Comparison among the PXRD patterns refined using the Rietveld method for the possible crystal system of S_2. a) Orthorhombic, b) Monoclinic and c) Cubic crystal system.

the orthorhombic crystallographic parameters are selected for the rietveld analyses for all of the obtained targets. Fig. 2 a-f shows the PXRD patterns of S_1 – S_6, respectively, based on the orthorhombic crystal system parameters. The data show that when the reaction time is increased from 10 h to 15 h, the purity of the obtained target is increased from 72 % to 100 %. The impurity phase is belonged to Bi_2O_3 crystal structure with space group $P2_1/c$ and the lattice parameters a = 5.84993 Å, b = 8.18493 Å and c = 7.50562 Å with β = 112.86938 ° [46]. Because the purity of the target was increased with increasing the reaction time to 15 h, the doping process was performed according to the reaction condition for the synthesis of S_2. The PXRD patterns of the doped materials are shown in Fig. 2 c-f. The ionic radii of Bi^{3+}, Sn^{4+}, Y^{3+}, Eu^{3+}, Gd^{3+} and Yb^{3+} are 1.17, 0.69, 1.019, 1.066,

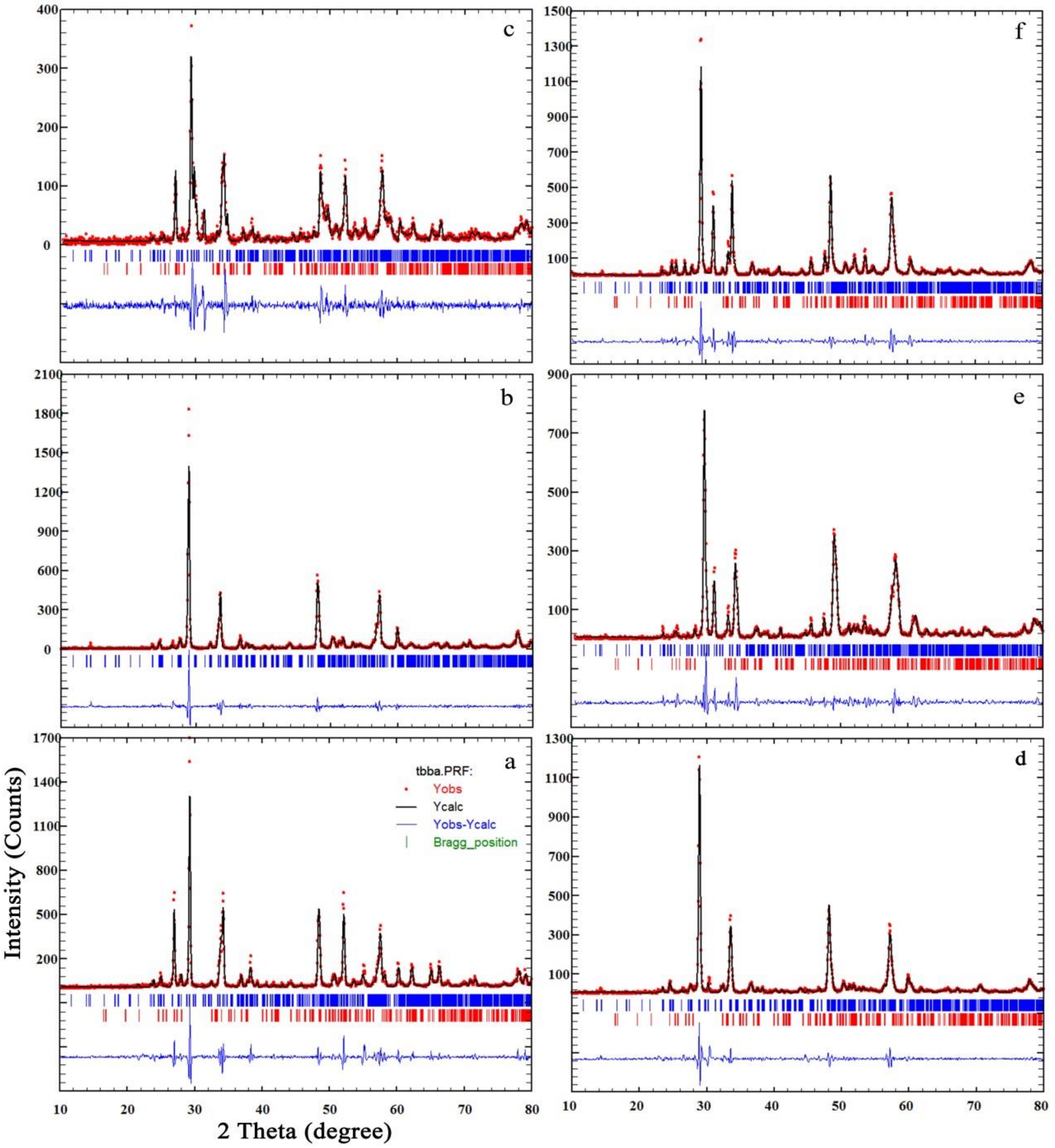

Fig. 2. PXRD patterns refined with the Rietveld analysis of a) S_1, b) S_2, c) S_3, d) S_4, e) S_5 and f) S_6.

Table 1. Comparison study for crystal system conformity for S_2.

Crystal system	R_F	R_{Bragg}	χ^2
Orthorhombic	1.10	1.53	2.00
Monoclinic	2.02	3.08	2.98
Cubic	3.60	4.97	17.5

1.053 and 0.985 Å, respectively. So, it is desirable for the crystal system to accept the dopant ions in the eight coordinated cavities. The intercalation in the A position is confirmed by calculating the unit cell volume of the doped materials. The data show that no considerable change in the unit cell

Table 2. Rietveld analysis and unit cell parameters data of the obtained nanomaterials.

Sample	**R_F**	**R_{Bragg}**	**χ^2**	**a**	**b**	**c**	**Volume (Å)^3**	**D_x**	**Counts**	**Purity(%)**
S_1	2.23	3.04	3.26	7.43443	21.44484	15.21620	2426	0.48	1723	72
S_2	1.10	1.53	2.00	7.54632	21.51632	15.08011	2439	0.47	1836	100
S_3	2.11	4.56	1.91	7.64699	21.10178	14.89042	2402	0.48	377	92
S_4	1.17	1.76	1.84	7.60161	21.33780	15.14071	2455	0.47	1204	95
S_5	2.17	3.61	2.29	7.66606	21.17765	14.92759	2423	0.48	746	94
S_6	1.80	2.60	2.54	7.67314	21.38833	14.84477	2436	0.47	1354	87

Table 3. Crystallite size, interplanar spacing, dislocation density and strain data of the obtained nanomaterials.

Sample	**2θ**	**B ()**	**B (rad)**	**cosθ**	**Sinθ**	**D (nm)**	**δ (lines/m^2)**	**ε**	**d_{Bragg} (Å)**	**d_{Calc} (Å)**
S_1	29.2105	0.25441	0.004438	0.967686	0.25216	32	9.76	1.07	0.31	3.08
S_2	28.9961	0.25415	0.004434	0.968156	0.25035	32	9.76	1.07	0.30	3.09
S_3	29.3357	0.27346	0.004770	0.967410	0.25321	31	10.41	1.15	0.30	3.05
S_4	28.9004	0.29085	0.005074	0.968365	0.24954	28	12.76	1.22	0.31	3.05
S_5	29.2554	0.29552	0.005155	0.967587	0.25234	28	12.76	1.25	0.31	3.05
S_6	29.2692	0.29112	0.005078	0.967557	0.25265	28	12.76	1.23	0.30	3.05

volume is observed. According to the PXRD data shown in Fig. 2, it is clear that there is no impurity peak related to the dopant ions. Table 2 shows the crystallographic parameters and the rietveld refinement data of the obtained materials. The data show that the doping processes proceed in a way that an impurity peak corresponded to Bi_2O_3 is observed. The impurity amount is varied when the dopant ion type is changed. The purity data of the obtained materials reveal that when the ionic radius of the dopant ion is close to the ionic radius of Bi^{3+}, the purity of the doped target is increased. So, the data show that when Yb^{3+} with the high difference is doped into the crystal system, the purity is decreased more. However, the purities of Y^{3+}, Gd^{3+} and Eu^{3+} - doped $Bi_2Sn_2O_7$ nanomaterials are high because the difference between the ionic radii of dopant ions and Bi^{3+} is small. Table 2 displays the rietveld analyses data of the obtained targets. The data show the goodness of the fittings. It is clear that the crystal phase growth (Counts) of the obtained targets has an important influence on the goodness of the fitting.

The crystallographic data of the obtained samples are calculated and compared to the observed data presented in Table 3.

Also, Table 3 shows the crystallite size data (D) of the obtained nanomaterials calculated by Scherrer equation:

$$D = \frac{K\lambda}{B_{\frac{1}{2}} cos\theta} \qquad (1)$$

In this equation, D is the entire thickness of the crystalline sample, λ is the X-ray diffraction wavelength (0.154 nm), K is the Scherrer constant (0.9), $B_{1/2}$ of FWHM is the full width at half its maximum intensity and θ is the half diffraction angle at which the peak is located. The interplanar spacing values calculated using Bragg equation was also included in Table 3. The value of the dislocation density δ [(lines/m^2)10^{14}], which is related to the number of defects in the crystal was calculated from the average values of the grain size (D) by the relationship given below:

$$\delta = \frac{1}{D^2} \qquad (2)$$

It was found that the dislocation density was increased when the dopant ions were introduced into the crystal system. However, the data show that doping the lanthanide ions into the crystal cavity increases the dislocation density considerably due to the decreasing the crystallite sizes of the materials. The strain ε (10^{-3}) values are also determined using the following formula:

$$\varepsilon = \frac{\beta_{hkl} cos\theta}{4} \qquad (3)$$

The variation in the strain as a function of the dopant ion type is included in Table 3. The increase in the strain value with changing the dopant ion is probably due to the retrograde in the degree of the crystallite of the obtained target. However, when Y^{3+} is doped into the crystal system, the strain value is

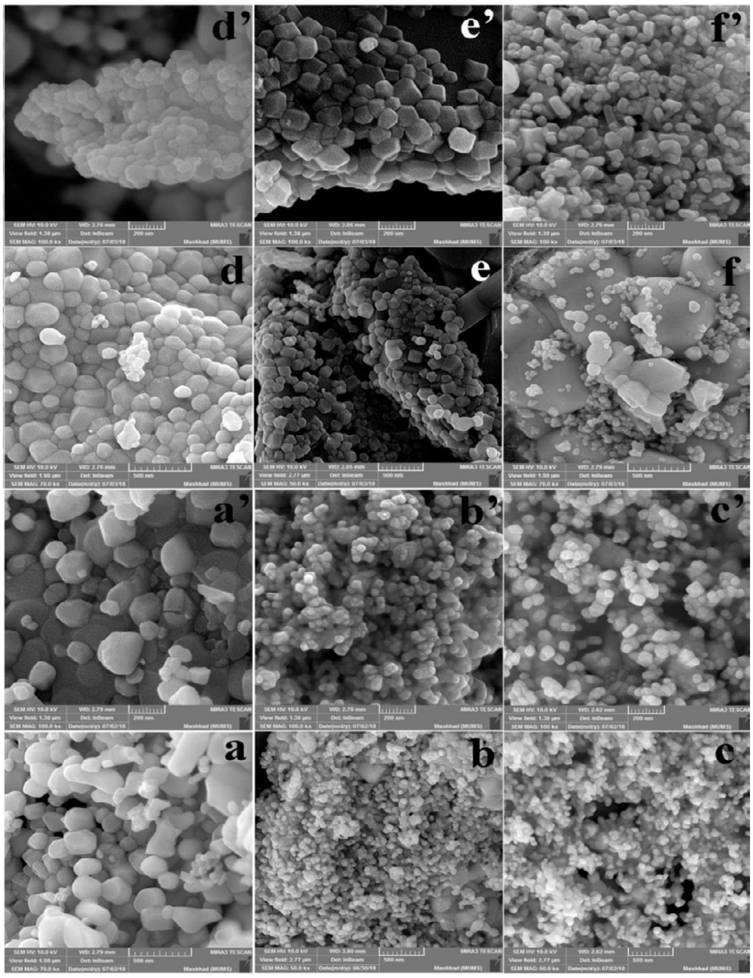

Fig. 3. FESEM images of a,a') S_1, b,b') S_2, c,c') S_3, d,d') S_4, e,e') S_5 and f,f') S_6.

small. Besides, when the lanthanide ions are doped into the crystal system, the strain value is increased. This is maybe due to the lanthanide contraction effect of 4f energy level on the crystallite size.

The X-ray density (D_x) is calculated using the following formula:

$$D_{x}=\frac{8M}{Na.b.c} \quad (4)$$

Where M is the molecular weight of $Bi_2Sn_2O_7$ (MW=867.34 $gmol^{-1}$), N is the Avogadro number, and *a, b and c are* lattice parameters (Table 2). The data show that the X-ray density value is small and is not changed considerably by changing the dopant ions. This can be due to the similar/smaller atomic weight of the dopant ions compared to Sn or Bi, respectively, and the incorporation of the small amount of the dopant ion into the crystal system.

The unit cell volume included in Table 2 can be obtained from the bellow formula:

$$V = a.b.c$$

The interplanar spacing can be calculated from the below formula:

$$\frac{1}{d^2}=\left(\frac{h^2}{a^2}+\frac{k^2}{b^2}+\frac{l^2}{c^2}\right)$$

The highest intensity peak at 2θ ≈ 28.90 º, the (h k l) value of (0 4 4) was used in the above equation.

So,

$$\frac{1}{d^2}=\left(\frac{16}{b^2}+\frac{16}{c^2}\right)$$

Fig. 3 shows the FESEM images of the obtained targets. Figs. 3 a,a' and b,b' show the FESEM images of S_1 and S_2, respectively. It is clear that

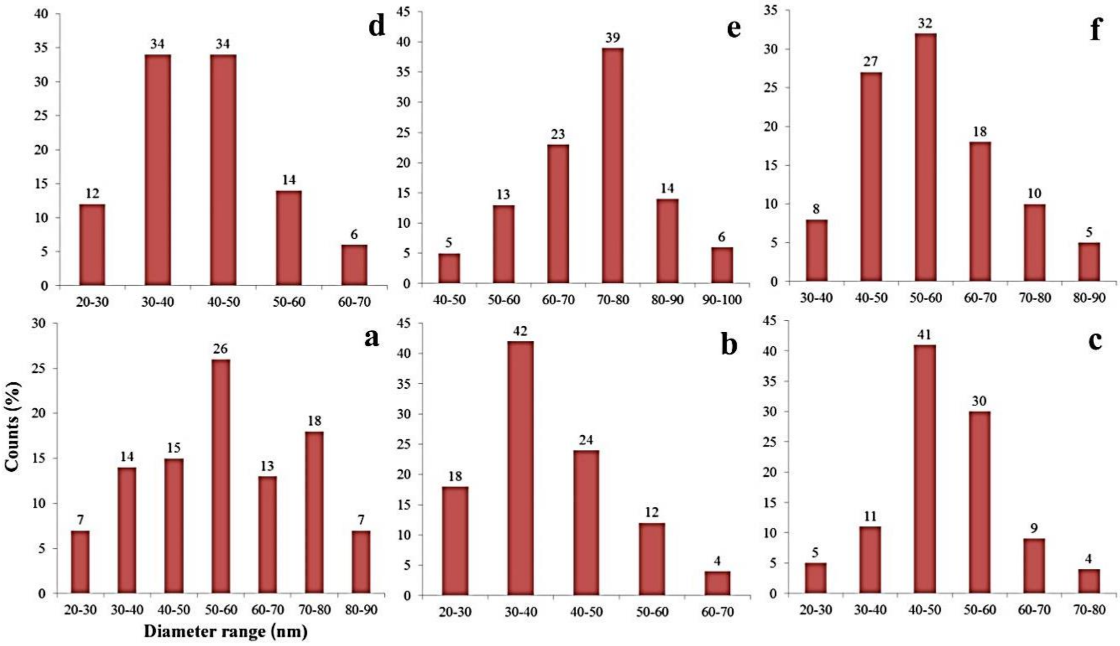

Fig. 4. Particle size distribution profiles of a) S_1, b) S_2, c) S_3, d) S_4, e) S_5 and f) S_6.

the morphology of the synthesized $Bi_2Sn_2O_7$ nanomaterials is particle. When the reaction time is increased to 15 h, the homogeneity of the particle size and morphology is increased. Besides, according to Figs. 4 a and b, the particle diameter size distribution of S_1 is in the range of 50-60 nm and S_2 is 30-40 nm. It is clear that increasing the reaction time has an important influence on the particle size of the targets. Figs. 3 c,c' to f,f' display the FESEM images of S_3-S_6. The images show that the morphology of the obtained materials is particle. However, there is a difference in the particle size homogeneity among the samples. The particle size distribution profiles showing the homogeneity of the obtained powders are shown in Fig. 4 c – f. The data show that when Y^{3+} is doped into the crystal system, the average particle size is in the range of 40-50 nm. However, the particle diameter sizes of S_4-S_6 are 30-50, 70-80 and 50-60 nm.

Fig. 5 (a - d) shows the EDX spectra of the obtained nanomaterials as a function of Y_2O_3, Eu_2O_3, Gd_2O_3 and Yb_2O_3 concentrations. The spectra indicated the X-rays emitted from various elements. The peaks corresponded to Y or Eu or Gd or Yb and (Bi, Sn and O) atoms present in the samples are labeled. The respective energy positions and the specific X-ray lines from various elements are also indicated. The Figure illustrates the EDX analyses for the samples doped theoretically with 0.02 mmol of the dopants into the crystal system which verifies the doping and the compositional analysis of Y^{3+} or Eu^{3+} or Gd^{3+} and/or Yb^{3+} in $Bi_2Sn_2O_7$. The normalized elemental analyses of the doped materials showed that the experimental formulas are $Bi_2Y_{0.012}Sn_2O_7$, $Bi_2Eu_{0.01}Sn_2O_7$, $Bi_2Gd_{0.012}Sn_2O_7$ and $Bi_2Yb_{0.016}Sn_2O_7$. It is clear that the capacity of the crystal system to accept the dopant ions is different. The data show that the capacity is increased when the ionic radius of the dopant is decreased. Because no obvious change in the unit cell volume value is observed when the dopant ions are doped into the crystal system, we can conclude that the ions are incorporated more into the Bi site. So, the dopant level of Yb^{3+} in the $Bi_2Sn_2O_7$ crystal system is highest compared to the other dopant ions.

Optical Property

The absorption spectra and direct optical band gap energies of the obtained $Bi_2Sn_2O_7$ and $Bi_2M_xSn_2O_{7+\delta}$ (M= Y, Eu, Gd and Yb) nanomaterials obtained from UV-Vis absorption spectra are shown in Fig. 4 a and b, respectively. According to the results of Pascual et al. [47], the relation between the absorption coefficient and incident photon energy can be written as $(\alpha h\nu)^n = A(h\nu - E_g)$, where A is a constant and E_g is the direct band gap energy if n=2. The Band gap energies were

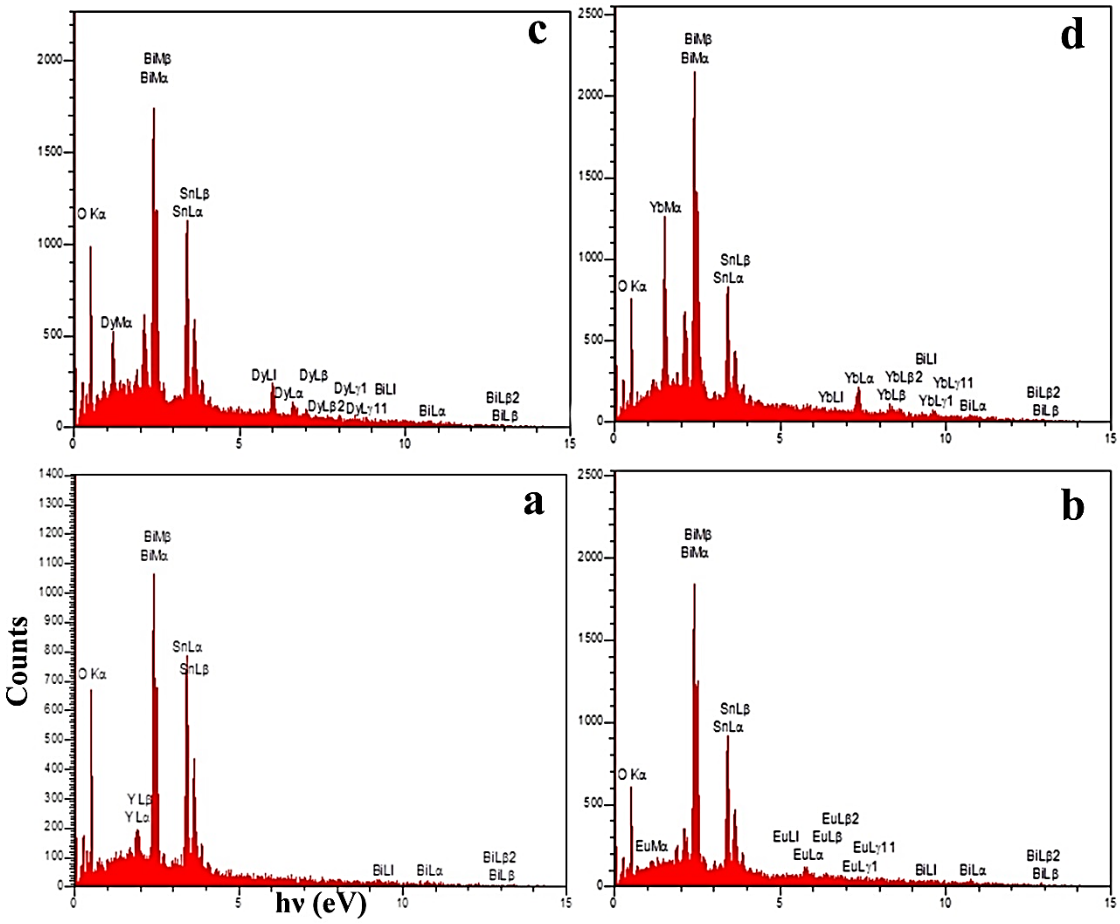

Fig. 5. EDX diagrams of a) S_3, b) S_4, c) S_5 and d) S_6.

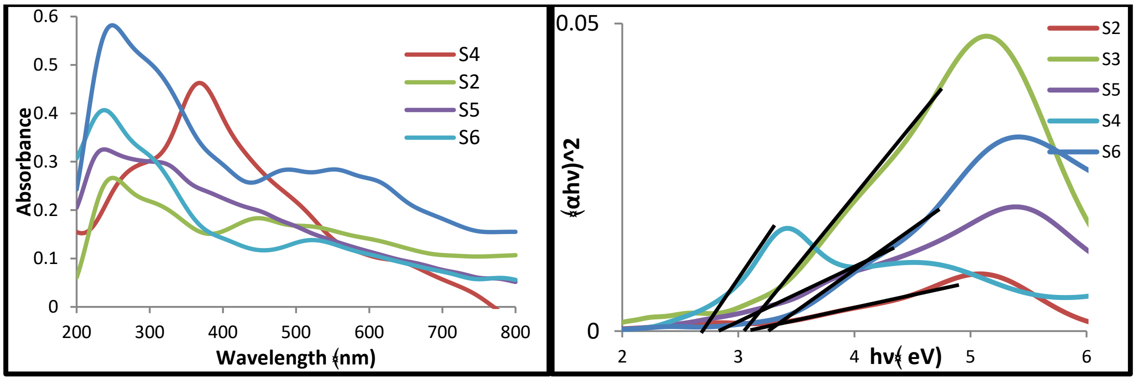

Fig. 6. Plots of a) UV-Vis spectra and b) direct band gap energies of the obtained materials.

evaluated from extrapolating the linear part of the curve to the energy axis. The direct optical band gaps were 3.20, 3.15, 2.75, 2.85 and 3.30 eV for S_2, S_3, S_4, S_5 and S_6, respectively. The data show that the band gap energy value for the pure material S_2 is 3.20 eV. The larger band gap energy compared to the other reported values [24] is due to decreasing the crystallite size of the pure $Bi_2Sn_2O_7$. The band gap energy values for Bi_2O_3, Y_2O_3, Eu_2O_3, Gd_2O_3 and Yb_2O_3 are 2.50 [48], 5.50 eV [49], 4.40 eV

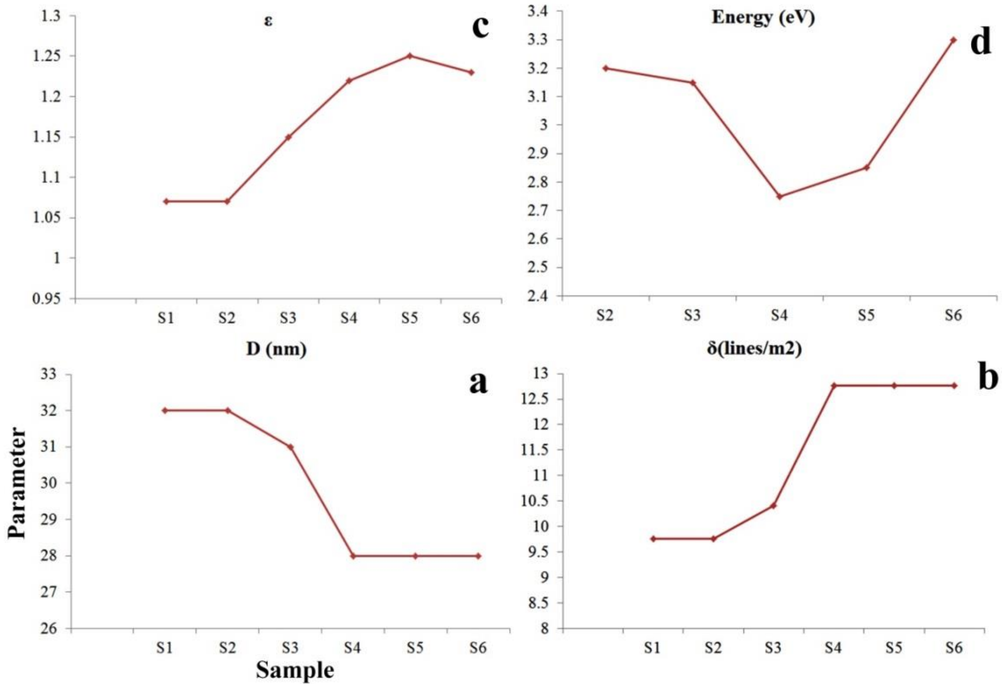

Fig. 7. Relations among different crystallographic parameters with optical band gap energy.

[50], 3.40 eV [51] and 4.90 eV [52]. The band gap values of the M_2O_3 are so larger than those of the pure and doped $Bi_2Sn_2O_7$ nanomaterials. So, the small band gap values of the as-prepared materials are due to the formation of composite materials Bi_2O_3 - $Bi_2M_xSn_2O_{7+\delta}$. It seems that in the composite materials, the influence of Bi_2O_3 on the band gap energy is more than the dopant ions.

Fig. 7 shows the Relations among different crystallographic parameters with the calculated direct optical band gap energies of the obtained materials. The data indicate that the ε and δ parameters show the apparent indirect relation with D value. Besides, there is an important observation with comparing E value with the other parameters. It is clear that E is related to the crystallite size in other words strain and dislocation density of the sample. With decreasing the crystallite size, the strain and dislocation density is increased and so the optical band gap energy is also increased. Increasing the band gap energy is due to increasing the difference between the energy levels of HOMO and LUMO. So, according to the observations, increasing the retrograding the crystal and dislocation density, the energy level difference is increased and so the band gap value is increased.

Photocatalytic activity

Experimental design for achieving optimal conditions in MG degradation process

There are two different approaches to optimize parameters affecting a chemical reaction, i.e., one-at-a-time and experimental design approaches. Experimental design is attracting attention in the literature for exploring the optimal level of the factors affecting chemical reactions, since they take into account all of the main and interaction effects with much smaller number of experiments. One of the most common designs is full factorial design [53,54].

Response surface methodology (RSM) is a mathematical and statistical method, which analyzes experimental design by applying an empirical model [53]. The adequacy of the applied model is checked using analysis of variance (ANOVA) [54]. The response is the measured degradation yield (Y %). Different possible combinations of catalyst amount, H_2O_2 volume and process time factors are designed and collected in Table 4. Here, four replicates at the center of factors were considered for the validation of the model by ANOVA (Table 6). All the experiments were done in two days in random order.

Table 4. Three-level full factorial design in photodegradation process.

	H_2O_2 (mL)	Catalyst (mg)	Time (min)	Yield (%)
Day 1	30	0.1	10	100
Day 1	20	0.075	25	98
Day 1	3	0.075	25	96
Day 1	20	0.075	25	98
Day 1	20	0.075	25	100
Day 1	10	0.05	40	97
Day 1	20	0.075	25	98
Day 1	37	0.075	25	100
Day 1	30	0.05	10	77
Day 1	10	0.05	10	24
Day 1	20	0.075	50	100
Day 1	20	0.03	25	60
Day 2	20	0.075	25	61
Day 2	20	0.075	25	92
Day 2	30	0.1	40	100
Day 2	20	0.075	1	4
Day 2	10	0.1	40	100
Day 2	30	0.05	40	100
Day 2	20	0.12	25	98
Day 2	10	0.1	10	47

Table 5. The experimental range and levels of independent variables in CCD.

Independent variables	Ranges and levels				
	Low Actual	High Actual	Low Coded	High Coded	Mean
(A) Catalyst (mg)	10	30	-1	1	20
(B) H_2O_2 (mL)	0.05	0.1	-1	1	0.075
(C) Time (min)	10	40	-1	1	25

Table 6. Analysis of variance for suggested model.

Source	**squares**	**df**	**Mean squares**	**F value**	**P value**	
Model	12694.2	5	2538.83	12.99	< 0.0001	significant
A-catalyst	980.66	1	980.66	5.02	0.0419	
B-H_2O_2	933.47	1	933.47	4.78	0.0464	
C-Time	7057.3	1	7057.3	36.1	< 0.0001	
AC	1326.12	1	1326.12	6.78	0.0208	
C^2	2396.61	1	2396.61	12.26	0.0035	
Residual	2736.84	14	195.49			
Lack of Fit	1608	9	178.67	0.79	0.6425	not significant
Pure Error	1128.83	5	225.77			
Cor Total	15431	19				

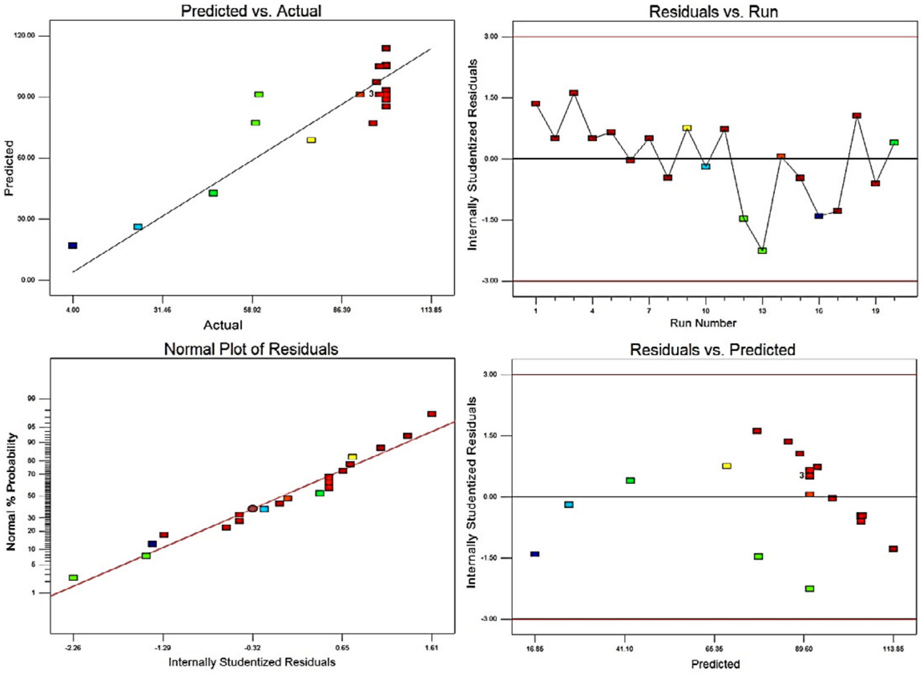

Fig. 8. Normal plot of residual, predicted versus actual, studentized residuals versus the run and predicted data plots for the photodegradation removal of MG.

The low and high factor levels are coded to -1 and +1, respectively. The below equation shows the relation between the factors and the yield of the reaction, Y%, based on the first-order model:

$$Y\ (\%) = -66.82663 + 2.99323 \times \text{catalyst} + 330.70025 \times H_2O_2 + 6.07206 \times \text{Time} - 0.085833 \times \text{catalyst} \times \text{Time} - 0.056798 \times \text{Time}^2$$

As could be seen from the ANOVA results listed in Table 6, the p-value of the regression was smaller than 0.05. This indicated that the model was significant at a high level of confidence (95%) [53]. The p-value probability of lack of fit was also greater than 0.05, which confirmed the significance of the model. Also, the coefficient of determination (the R-square, adjusted–R-square) was used to express the quality of fit of polynomial model equation. In this case, R^2 value of variation fitting for Y% = 100 indicated a high degree of correlation between the response and the independent factors ($R^2 = 0.82$). The high value of adjusted regression coefficient (R^2-adj = 0.76) was also another index for the high significance of the proposed model. This means that the difference between the experimental and predicted responses was negligible. Also, the predicted R-squared value (0.63) was reasonable which indicated the high accuracy and reliability of the developed model in the determination of response values shown in Fig. 8. As it is evident in this figure, the data points obtained consistently appear on a straight trend line, demonstrating that there is no obvious dispersal. The dispersal of residuals is also shown in Fig. 8. It is clear that the residuals are in the range of -3 to +3 confirming more the reliability of the model.

To illustrate the effects of the factors in the above models, the two and three–dimensional response surface plots of the response are shown in Fig. 9. The Figure represents the 3D and counter plots related to the interaction of AC in which A is the amount of catalyst and C is the reaction time. The semi-curvature of the plot indicates the interaction between the variables. In other words, when the time and catalyst amount increase, dye removal percentage improves. This means that the mass transfer of MG molecules is enhanced when the surface area of the catalyst is increased. So, the dye removal process on the catalyst surface is reached to equilibrium state quickly. Besides, by increasing the catalyst amount, further surface area of catalyst is available for dyes molecules enhancing the dye removal yield.

Fig. 10 shows the residual data obtained for

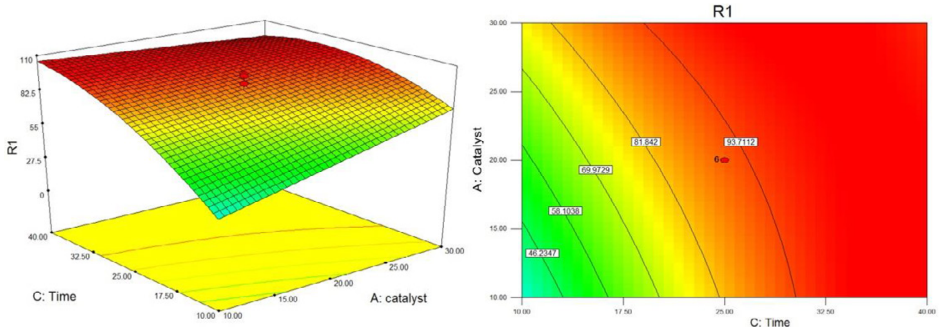

Fig. 9. 2 D and 3D surface plots of MG dye removal.

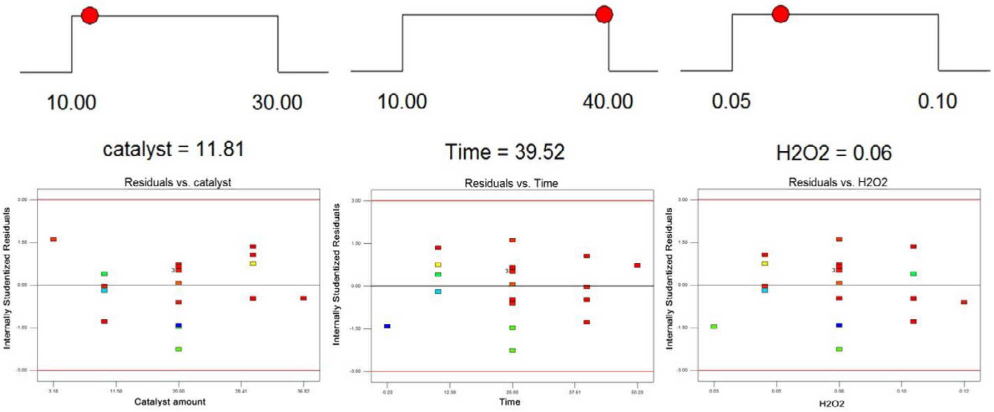

Fig. 10. Dispersial residual data for each parameter and the optimum values for each parameter.

each parameter associated with the optimum value obtained by the mentioned model. The data show that the dispersal residuals are in the range. Besides, the data show that the optimum values for catalyst, H_2O_2 and time are 12 mg, 0.06 mL and 40 min, respectively.

In the present work, the central composite design (CCD) was chosen for modeling and optimization of the proposed procedure based on the as-synthesized nanocatalyst (S_1). A three-level CCD with three factors (H_2O_2 (A), catalyst (B) and time (C)) was used to investigate the effects of factors. The experimental range and levels of independent variables are shown in Table 4. The condition of 20 experiments designed by CCD accompanied to dye degradation percentage (response (R%)) is also given in Table 4. As shown in Table 5, the independent variables (H_2O_2 volume (A), catalyst amount (B) and stirring time (C)) are given the coded form (-α, -1, 0, +1, +α).

To prepare 40 ppm of MG solution, 10 mg of MG powder was dissolved in 250 mL of distilled water. The pH value of the obtained solution was 4. To increase the pH value, we used a 0.01 M NaOH solution. According to the Table 4, in a typical experiment, certain amount (g) of the as-synthesized $Bi_2Sn_2O_7$ (S_1) photocatalyt was added into 50 mL of MG solution and sonicated for 10 min in a dark room to establish an adsorption/desorption equilibrium between MG molecules and the surface of the photocatalyst. Afterward, certain volume (mL) of H_2O_2 was added into the mixture solution followed by further magnetic stirring under solar light. When the designed time (min) was elapsed, the solution was drawn out and the photocatalyst was separated by centrifugation in order to measure the absorption spectrum of MG and calculate the MG concentration using UV-Vis spectroscopy. The photodegradation (%) of MG was calculated by the following formula:

$$\left(\frac{A_0\text{-}A_t}{A_0}\right)\times 100 \qquad (3)$$

where, A_0 and A_t represent the initial absorbance

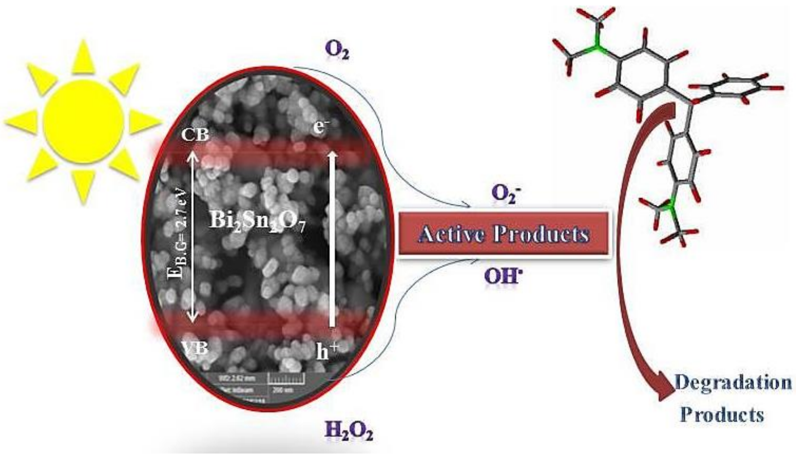

Scheme 1. The general process for the photocatalytic degradation of malachite green.

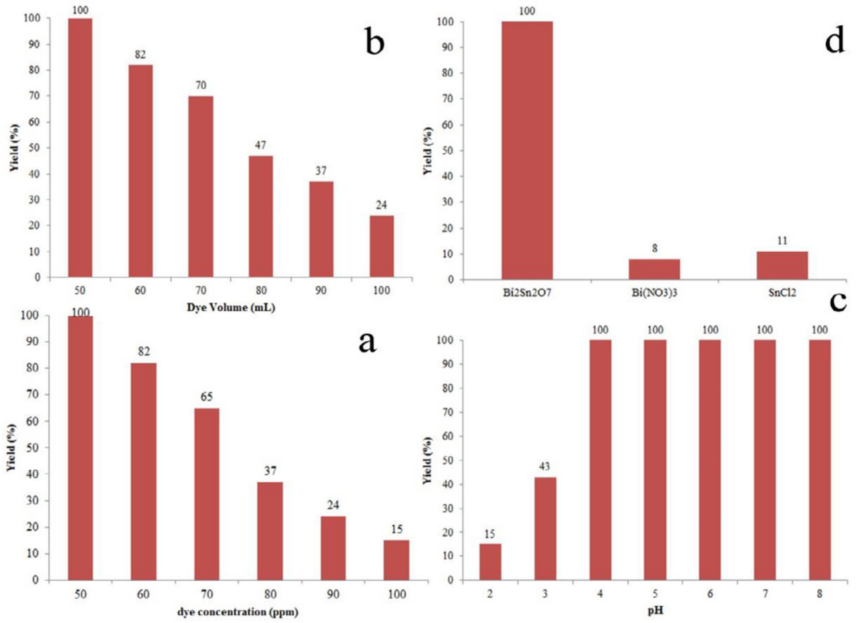

Fig. 6. MG degradation (%) at different (a) dye concentrations, (b) dye volumes, (c) dye pH values and (d) comparison tests among the raw materials and $Bi_2Sn_2O_7$.

of MG at 612 nm and the absorbance at time t, respectively.

Scheme 1 presents the general procedure for the photocatalytic degradation of MG by the as-synthesized nanomaterials.

Fig. 6 shows the dye degradation graphs for the obtained material at the optimum conditions. Fig. 6 a shows the effect of dye concentration on the degradation yield. It is clear that when the dye concentration is increased more up to 60 ppm, the degradation is decreased. It seems that when the dye concentration is high, light wavelength can not penetrate into the dye solution and the photocatalytic activity cannot be started efficiently. Fig. 6 b shows the dye volume effect on the degradation yield. It indicates that the degradation is complete when dye volume is 50 mL; when the volume the dye volume is increased up to 70 mL, the yield is decreased, considerably. It is due to the decreasing the adsorption of dye on the catalyst; so the process is continued slowly at the desired time. Fig. 6 c shows the effect of pH value

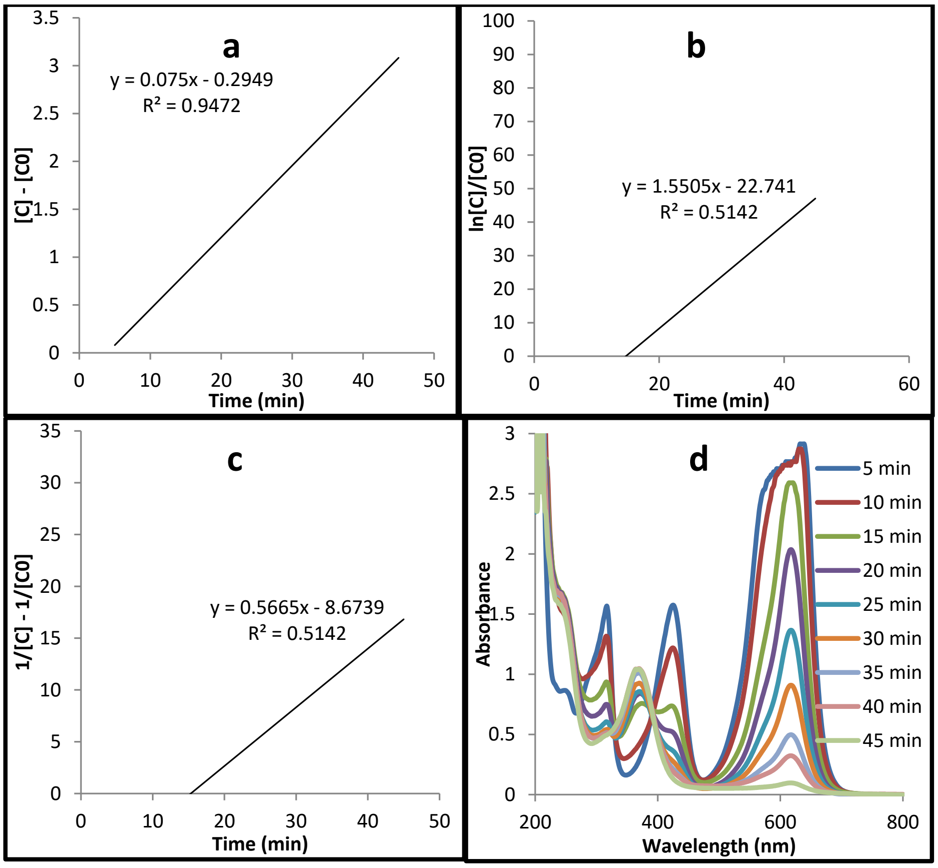

Fig. 7. Plots of a) [C] – [C_0], b) ln ([C_0]/[C]), c) 1/[C] – 1/[C_0] versus irradiation time and d) UV-visible absorption spectra for MG degradation.

on the degradation yield. Fig. 6 c shows that the degradation yield is small at pH values up to 3. However, when the pH is increased up to 10, the degradation yield is increased. The yield is 100% at pH=4 to 10. It is due to the increased amount of OH^- ion in the solution. Fig. 6 d shows the comparison among the raw materials and the as-synthesized nanomaterial for the degradation yield. It shows that $Bi_2Sn_2O_7$ efficiency for removal of MG is so higher than those for raw materials.

Kinetic study

Studying the reaction kinetics is important for appointing the parameters affecting the reaction rate. This study finds a suitable kinetic model for the photo-catalytic degradation reaction. For this purpose, the rate constant (k) and the correlation coefficient (R^2) of dye degradation is studied by zero- (Eq. (1)), first- (Eq. (2)), and second-order (Eq. (3)) kinetics.

$$[C]=-k_0\,t+[C]_0 \qquad (1)$$

$$\ln [C]_0/[C] =k_1\,t \qquad (2)$$

$$1/[C] -1/[C]_0 =k_2\,t \qquad (3)$$

where C is the MG concentration in an aqueous solution at time t; C_0 is the initial MG concentration; and k_0 (mg. $L^{-1}min^{-1}$), k_1 (min^{-1}), and k_2 (L .$mg^{-1}min^{-1}$) are the zero-, first-, and second-order rate constants, respectively. The results showed that the kinetics of the degradation using $Bi_2Sn_2O_7$ followed a zero-order kinetic model.

By plotting **[C] - [C_0]** versus t, a straight line was obtained (Fig. 7). The slope of this line represents the apparent rate constant (k_{app}). Fig. 7 shows that the photo-catalytic degradation fits to the Langmuir–Hinshelwood kinetic model. As a result of the data, the kinetic of degradation followed a pseudo-zero-order kinetic model. The amount of R^2 and k_{app} are 0.075 and 0.972 for the dye concentrations of MG, respectively.

To show the merit of the present work with the other reported photocatalytic degradation

Table 7. Comparison study for the degradation efficiency [44].

Catalyst	Condition	Yield (%)
$Bi_2Sn_2O_7$(Present work)	H_2O_2, 12 mg catalyst, 40 min, Natural ligth, 50 mL and 40 ppm MG	100
Carbon/TiO_2	25 ppm MG, 30 min, pH=8	82-100
MoS_2/TiO_2	40 min, sunlight irradiation, 0.1 g catalyst, 10 ppm MG	97
$PbCrO_4$	365 ppm MG, 0.1 g catalyst, 4 h, pH=7.5, visible light, 60 min	90
$Ni_{1-x}Co_xFe_2O_4$	Sunlight, 50 mL solution, 25 ppm catalyst, 1 µM MG, H_2O_2, 15 h	100
Mg-doped TiO_2	Visible light, pH=9, 100 ppm MG	89
ZnO	4h time, 60 ppm MG, pH=7.5, solar radiation	98
$FeSO_4$ -$7H_2O$	10 mM Fe2+, 40 °C, 25.5mM H_2O_2, 10 ppm MG	94
$Sr_2As_2O_7$	H_2O_2, 20 mg catalyst, 33 min, 70 mL of 100 ppm MG, solar light	97

researches, we present a copmarison study among the yield in the present work with the other catalysts (Table 7).

CONCLUSION

The present work reported the synthesis of $Bi_2Sn_2O_7$ and $Bi_2M_xSn_2O_7$ (M= Y^{3+}, Eu^{3+}, Gd^{3+} and Yb^{3+}) nanomaterials via a one-step solid state method at 800 °C for 10 and 15 h. PXRD data showed that $Bi_2Sn_2O_7$ was crystallized well in orthorhombic crystal system. Rietveld analysis data showed that when the reaction time was 15 h, the purity of the obtained target reached 100 %. The doping process was performed according to the reaction condition and the influence of the dopant ions on the particle size and optical band gap energy was studied. EDX analysis data revealed that dopant ion type had an important influence on the crystal system capacity to site the ions in the A or B position. The data showed that the obtained $Bi_2Sn_2O_7$ nanomaterial had excellent efficiency for the removal of MG from aqueous solution. It was found that the optimum condition was 0.06 mL H_2O_2, 12 mg catalyst and 40 min. The degradation yield at the optimum condition was 100 % for S_1. Several tests were performed for investigating the effect of different parameters on the degradation yield. It was found that the catalytic performance was excellent when the pH value was in the range of 4 to 10, the dye concentration was up to 60 ppm and the dye volume was up to 60 mL. The photo-catalytic degradation data showed that the kinetic of degradation followed a pseudo-zero-order kinetic model. The amount of R^2 and k_{app} are 0.075 and 0.972 for the dye concentrations of MG, respectively.

CONFLICT OF INTEREST

The authors declare that they have no conflict of interest.

REFERENCE

[1] S. Khademinia, M. Behzad, H. Samari Jahromi, RSC Adv. 5, 24313 (2015).
[2] S. Khademinia, M. Behzad, Adv. Powder Tech. 26, 644 (2015).
[3] S. Khademinia, M. Behzad, L. Kafi-Ahmadi, S. Hadilou, Z. Anorg. Allg. Chem. 644, 221 (2018).
[4] R S. Roth, J. Res. Natl. Bur. Stand. 56, 17 (1956).
[5] A. Salamat, A.F. L Hector, P. McMillan, C. Ritter, Inorg. Chem. 50, 11905 (2011).
[6] W. Huang, C. Hu, B. Zhu, Y. Zhong, H. Zhou, Adv. Eng. Res. 146, 309 (2018).
[7] Q. Tian, J. Zhuang, J. Wang, L. Xie, P. Liu, Appl. Catal. A: General. 425-426, 74 (2012).
[8] Y. Xing, X. Yin, Q. Que, W. Que, J. Nanosci. Nanotech. 18, 4306 (2018).
[9] W. Xu, Z. Liu, J. Fang, G. Zhou, X. Hong, S. Wu, X. Zhu, Y. Chen, C. Cen, Int. J. Photoenergy. http://dx.doi.org/10.1155/2013/394079.
[10] P.C. Andrews, P.C. Junk, I. Nuzhnaya, D.T. Thielemann, Inorg. Chem. 51, 751 (2012).
[11] J. Wu, F. Huang, X. Lu, P. Chen, D. Wan, and F. Xu, J. Mater. Chem 21, 3872 (2011).
[12] M.C. Long, W.M. Cai, J. Cai, B.X. Zhou, X.Y. Chai, Y.H. Wu, J. Phys. Chem. B. 110, 20211 (2006).
[13] A. M. Ali, E. A. C. Emanuelsson, and D. A. Patterson, Appl. Catal. B: Env. 97, 168 (2010).
[14] Z.G. Zou, J.H. Ye, K. Sayama, H. Arakawa, Nature. 41, 625 (2001).
[15] K.R. Raghava, M. Hassan, V.G. Gomes, Appl. Catal. A Gen. 489, 1 (2015).
[16] Z.J. Zhang, W.Z. Wang, L. Wang, S.M. Sun, Mater. Interfaces. 4, 593 (2012).
[17] J. Wu, F. Huang, X. Lu, P. Chen, D. Wan, F. Xu, J. Mater. Chem. 21, 3872 (2011).
[18] Q.F. Tian, J.D. Zhuang, J.X. Wang, L.Y. Xie, P. Liu, Appl. Catal. A Gen. 425, 74 (2012).
[19] J. Yang, J. Dai, J. Li, Appl. Surf. Sci. 257, 8965 (2011).
[20] C.H. Hu, X.H. Yin, D.H. Wang, Y. Zhong, H.Y. Zhou, G.H. Rao, Chin. Phys. B 25, 067801 (2016).
[21] J.W. Lewis, J.L. Payne, R.I. Evans, H.T. Stokes, B.J. Campbell, J.S.O. Evans, J. Am. Chem. Soc. 138, 8031 (2016).
[22] M. Roy, I. Bala, S.K. Barbar, J. Therm. Anal. Calorim. 110, 559 (2012).
[23] L. Moensa, P. Ruizb, B. Delmonb, M. Devillersa, Appl. Catal. A: Gen. 171, 131 (1998).
[24] M. Khairy, M. Mohamed, M. Phys. Chem. Chem. Phys. 17, 21716 (2015).

[25] J.J. Wu, F.Q. Huang, X.J. Lu, Mater. Chem. 21, 3872 (2011).
[26] Q.F. Tian, J.D. Zhuang, J.X. Wang, L.Y. Xie, P. Liu, Appl. Catal. A Gen. 425, 74 (2012).
[27] L. Moensa, P. Ruizb, B. Delmonb, M. Devillers, Appl. Catal. A Gen. 180, 299 (1999).
[28] J.J. Wu, F.Q. Huang, X.J. Lu, P. Chen, D.Y. Wan, F.F. Xu, J. Mater. Chem. 21, 3872 (2011).
[29] D. Li, J. Xue, New J. Chem. 39, 5833 (2015).
[30] J. Zhuang, C. Hu, B. Zhu, Zhong, H. Zhou, Earth Environ. Sci. 52, 012081 (2017).
[31] I. Bala, M. Roy, S.K. Barbar, S. Sahu, Solid State Phys. 1447, 997 (2012).
[32] H.W. Kim, S.H. Shim, J.W. Lee, J.Y. Park, S.S. Kim, Chem. Phys. Lett. 456, 193 (2008).
[33] I.R. Evans, J.A.K. Howard, J.S.O. Evans, J. Mater. Chem. 13, 2098 (2003).
[34] B.J. Kennedy, Ismunandar, M.M. Elcombe, Mater. sci. forum. 278-281, 762 (1998).
[35] R.D. Shannon, J.D. Berlein, J.L. Gillson, G.A. Jones, A.W. Sleight, J. Phys. Chem. Solids. 41, 117 (1980).
[36] R.X. Silva, C.W.A. Paschoal, R.M. Almeida, C.J.M. Carvalho, P. Ayalac, J.T. Auletta, M. W. Lufaso, Vib. Spectrosc. 64, 172 (2013).
[37] L.V. Udo, S.S. Aplesnin, M.N. Sitnikov, E.V. Eremin, M.S. Molokeev, Solid State Phenom. 233-234, 105 (2015).
[38] A. Walsh, G.W. Watson, D.J. Payne, G. Atkinson, R.G. Egdell, J. Mater. Chem. 16, 3452 (2006).
[39] S. Srivastava, R. Sinha, D. Roy, Aquat. toxicol. 66, 319 (2004).
[40] J. Tolia, M. Chakraborty, Z. Murthy, Pol. J. Chem. Technol. 14, 16 (2012).
[41] C. Chen, C. Lu, Y. Chung, J. Jan, J. Hazard. Mater. 141, 520 (2007).
[42] H.S. Kusuma, R.I. Sholihuddin, M. Harsini, H. Darmokoesoemo, J. Mater. Env. Sci. 7, 1454 (2016).
[43] K.H. Hu, M. Meng, Asian J. Chem. 25, 5827 (2013).
[44] F. Yousefzadeh, L. KafiAhmadi, S. Khademinia, Catal. Lett. 149, 1660 (2019).
[45] W. Xu, J. Fang, Y. Chen, S. Lu, G. Zhou, X. Zhu, Z. Fang, Mater. Chem. Phys. 154, 30 (2015).
[46] M. Sabaghian, M. Behzad, S. Khademinia, J. Appl. Chem. 11, 23 (2017).
[47] J. Pascual, J. Camassel, M. Mathieu, Phys. Rev. B Solid State. 18, 5606 (1978).
[48] L. Yin, Y. Dai, J. Niu, Mater. Lett. 92, 372 (2013).
[49] C.C. You, T. Mongstad, J.P. Maehlen, S. Karazhanov. Appl. Phys. Lett. 105, 031910 (2014). https://doi.org/10.1063/1.4891175.
[50] A. Prokofiev, A. Shelykh, B. Melekh, J. Alloys Compd. 242, 41 (1996).
[51] M. Pattabi, G. Arun Kumar Thilipan, AIP Conference Proceedings 1512, 726 (2013).
[52] S. Kimura, F. Arai, M. Ikezawa, J. Phys. Soc. Jpn. 69, 3451 (2000).
[53] Comprehensive Chemometrics Chemical and Biochemical Data Analyses, Vol. 1 (2009) chapter 12, page 354.
[54] G.E.P. Box, N.R Draper, Empirical model-building and response surfaces. Wiley: New York (1987).